Chemical Vapor Synthesis of Size-Selected Zinc Oxide Nanoparticles

*Sebastian Polarz, Abhijit Roy, Michael Merz, Simon Halm, Detlef Schröder, Lars Schneider, Gerd Bacher, Frank E. Kruis, and Matthias Driess**

ZnO can be regarded as one of the most important metal oxide semiconductors for future applications. Similar to silicon in microelectronics, it is not only important to obtain nanoscale building blocks of ZnO, but also extraordinary purity has to be ensured. A new gas-phase approach to obtain size-selected, nanocrystalline ZnO particles is presented. The tetrameric alkyl-alkoxy zinc compound $[CH_3ZnOCH(CH_3)_2]_4$ is chemically transformed into ZnO, and the mechanism of gas-phase transformation is studied in detail. Furthermore, the morphological genesis of particles via gas-phase sintering is investigated, and for the first time a detailed model of the gas-phase sintering processes of ZnO is presented. Various analytical techniques (powder XRD, TEM/energy-dispersive X-ray spectroscopy, magic-angle spinning NMR spectroscopy, FTIR spectroscopy, etc.) are used to investigate the structure and purity of the samples. In particular, the defect structure of the ZnO was studied by photoluminescence spectroscopy.

Keywords:
- gas-phase reactions
- nanocrystalline materials
- semiconductors
- single-source precursors
- zinc oxide

1. Introduction

Nanostructures, that is, structures with at least one dimension less than 100 nm, have received steadily growing interest as a result of their fascinating properties.[1–6] There are two main reasons for alterations in properties: increased interface area, and the dominance of quantum size effects. An understanding of the effects due to miniaturization, their influence on the properties of materials, and the exploitation of these effects for the design of structures, devices, and systems with novel properties and functions are the major goals of contemporary nanoscience and nanotechnology. Besides metallic quantum dots, nanoparticles of transition-metal oxides are of high interest because variations in the morphology (size and shape), composition, and valence state of metals, as well as defect structures in the oxygen lattice, allow one to tune the electrical, optical, magnetic, mechanical, and last but not least, the chemical properties.

Among different wide-bandgap semiconductors, zinc oxide (ZnO) is a key engineering material on it own merits. ZnO is a direct-bandgap semiconductor ($E_g = 3.37$ eV at low temperature; 3.30 eV at room temperature) with a free exciton binding energy of 60 meV, which ensures exciton emission at room temperature and above. This makes ZnO an excellent material for UV-light-emitting diodes (LEDs) and lasers.[7–9] ZnO is also used in solar cells,[10–12] field-emission displays, highly efficient green phosphor,[13] UV photodetectors,[14] gas sensors,[15] varistors,[16] and catalysts.[17]

It is envisaged that enhancement of properties would occur on decreasing the particle size into the nanometer

[*] Dr. S. Polarz, Dr. M. Merz, Dr. D. Schröder, Prof. M. Driess
Institute of Chemistry, Technical University Berlin
Strasse des 17. Juni 135, 10623 Berlin (Germany)
Fax: (+49) 30-314-22168
E-mail: matthias.driess@tu-berlin.de
Dr. A. Roy, F. E. Kruis
Process and Aerosol Measurement Technology
Department of Electrical Engineering and Information Technology
University Duisburg-Essen, 47057 Duisburg (Germany)
S. Halm, L. Schneider, Prof. G. Bacher
Department of Electrical Engineering and Information Technology
University Duisburg-Essen
Bismarckstrasse 81, 47057 Duisburg (Germany)

DOI: 10.1002/smll.200400085

NANO MICRO small

range, so a great deal of effort has been made to synthesize nanostructured ZnO and to understand the resulting properties (see one of the recent reviews).[18,19] Thus, enormous efforts have been undertaken to gain control over the morphology and chemical features of ZnO nanoparticles by various techniques, for example, colloidal methods.[20–24] Although colloidal routes offer some control of particle size, the presence of unwanted chemical species on the particle surface influences the resulting properties. This is of great concern for practical use. Attempts have been made to remove the reactants and reaction products by washing.[24] The question about the purity of the particles still remains, as some adsorbed species are strongly attached to the surface.[25] Some adsorbed species can be removed by thermal treatment; however, this leads to agglomeration as well as reaction of the adsorbed species with the surface of the nanoparticles.[25] This problem could hinder insights into the intrinsic properties of ZnO nanoparticles. Moreover, it seems rather difficult to derive samples with a particular particle size.

In this respect, gas-phase synthesis routes possess several advantages which could provide better control over particle morphology and crystallinity, and in addition allow continuous processing.[26] However, true gas-phase routes have seldom been reported, and are even less studied in detail and understood. The flame pyrolysis of solutions containing ZnO precursors was performed by different groups,[27] but neither the absence of impurities (from the solvent) nor a homogeneous distribution of particle morphology (size and shape) could be achieved. The evaporation and oxidation of elemental zinc at elevated temperature is the method of choice for the industrial production of ZnO. This method leads to inhomogeneous particle morphologies as well,[15,28] and details about processes during the gas-phase synthesis of metal oxide nanoparticles are still scarce.

In spite of huge activity toward the synthesis of nanostructured ZnO, a simple method for the formation of impurity-free ZnO nanoparticles with controlled morphology remains an important challenge. The present work is devoted to the gas-phase synthesis of pure, poly- and monodisperse nanocrystalline ZnO particles by chemical means (chemical vapor synthesis, CVS) using a volatile organometallic ZnO precursor. CVS is performed at higher process temperatures, higher precursor partial pressure, and longer residence time than chemical vapor deposition (CVD), thus resulting in particle formation.[29,30] The clear advantage of using molecular organometallic precursors in the CVS process over ionic precursors is that the former have a significantly higher vapor pressure and lower decomposition temperatures, which enable the formation of initially very small particles. Several organometallic precursors are reported in the literature for metal–organic chemical vapor deposition (MOCVD) of ZnO thin films.[31] In this context, the formation of ZnO nanoparticles from dimethylzinc reported by Roth et al. deserves attention.[32] They prepared ZnO from $Zn(CH_3)_2$ in a low-pressure H_2/O_2/Ar flame reactor as well as in an Ar/O_2 microwave plasma reactor, and investigated the particle formation process in situ by particle mass spectrometry. However, no detailed investigation has been performed on the size-classified nanoparticles.[32] The use of dimethylzinc as a precursor for zinc oxide has some inherent disadvantages: dimethylzinc is a very reactive compound toward oxygen and moisture which spontaneously burns in air. This makes it not only difficult to handle, but also difficult to perform reactions in a controlled manner.

Here, we report a detailed investigation of the CVS of ZnO nanoparticles using the volatile organometallic precursor $[CH_3ZnOCH(CH_3)_2]_4$ (subsequently denoted "heterocubane"). This precursor has the advantages that it is easily accessible, even on the multigram scale, and can be handled in air. It is interesting to note that a similar precursor containing ethylzinc groups instead of methylzinc was recently used to prepare ZnO particles by a colloidal method using surfactant.[33] In this paper, we explore the fundamental differences between the solid-state versus the gas-phase chemistry of the precursor $[CH_3ZnOCH(CH_3)_2]_4$. This allows for the first time the detailed investigation of the formation of ZnO agglomerates in the gas phase from a chemical point of view. In addition, their in-flight sintering was studied quantitatively. Thus, ZnO particles with controlled morphology, high crystallinity, and high purity have been obtained. Furthermore, the physical properties of the resulting ZnO particles are studied by various spectroscopic techniques. In particular, the photoluminescence (PL) properties and related defect structures of ZnO are reported.

2. Results and Discussion

To obtain ZnO materials of high purity, the following requirements have to be fulfilled for a good precursor: it should be readily available in bulk amounts, it should be simple to purify, evaporation needs to occur at temperatures significantly lower than its decomposition point, and last but not least, it should give ZnO directly without unwanted by-products.

We decided to apply an alkyl-alkoxy zinc compound with heterocubane architecture as a precursor, and first investigated its properties. In particular, the methylzinc isopropoxide $[CH_3ZnOCH(CH_3)_2]_4$ cluster, which has a central Zn_4O_4 framework, appeared to be a suitable molecular precursor for the formation of ZnO via simple elimination of propene and methane at a relatively low temperature. Its X-ray structure was determined for the first time (cell parameters $a=7.838(4)$; $b=9.468(6)$; $c=17.870(11)$ Å; $\alpha=77.457(12)$; $\beta=77.806(19)$; $\gamma=73.211(12)°$; $V=1223.5(13)$ Å^3; $R=3.5\,\%$; Cambridge Crystallographic Data Centre file CCDC 259836; www.ccdc.cam.ac.uk/data request/cif). In the current work we address the following points:

- Detailed study of the decomposition behavior and mechanism of the heterocubane.
- Investigation of the ZnO particle growth in the gas phase.
- Investigation of the purity of the CVS samples.

2.1 Decomposition Behavior of the Heterocubane

To obtain a first impression about the decomposition of $[CH_3ZnOCH(CH_3)_2]_4$, thermogravimetric analysis (TGA) was performed under an inert atmosphere (solid-state synthesis; SSS). At 200 °C, 91 % of the initial mass was lost, a fact which can only be explained by significant sublimation of the heterocubane at ambient pressure. However, there was no separate decomposition stage visible, and a brownish-black powder containing ZnO (according to powder X-ray diffraction, PXRD) as well as significant amounts of elemental carbon were obtained. It can be concluded that inert atmospheric conditions are suitable to bring the heterocubane into the gas phase, but its conversion into pure ZnO cannot be achieved this way. To gain more knowledge about the sublimation behavior of the heterocubane, its vapor pressure p was determined using a membrane-zero manometer (see Figure 1a and refs. [34, 35]). At temperatures between 60 and 180 °C, a linear decrease of p (plotted in logarithmic scale) against $1/T$ is observed. At lower temperatures (below 40 °C), practically no heterocubane is present in the gas phase, and at higher temperatures (above 180 °C), in agreement with TGA, decomposition of the precursor takes place which leads to a strong increase in pressure. If, in a separate experiment, the heterocubane is held at a temperature higher than 50 °C for a prolonged time (24–48 h), a slow but continuous increase of pressure is observed. This means that besides evaporation, above a certain temperature barrier simultaneous decomposition takes place. However, we conclude that this is due to solid-state decomposition, as the intact heterocubane can be fully recondensed from the gas phase. These investigations show that the sublimation of the heterocubane is determined by kinetic factors. This finding, and the fact that the total pressure is also influenced by gaseous products from the SSS, prevents the determination of thermodynamic parameters such as the sublimation enthalpy. It is nevertheless possible to control the amount of heterocubane in the gas phase by adjusting the temperature. The occurrence of significant amounts of carbon if the heterocubane is decomposed in argon could be a major drawback for the use of this precursor in CVS. Therefore, we investigated whether the quality of the products can be increased if the heterocubane is decomposed in an atmosphere containing oxygen (20 % O_2 + 80 % Ar). Under TGA conditions (see Figure 1b), a slow decrease in mass (1.6 %) was detected between 70 and 130 °C, which can be attributed to the sublimation of the heterocubane. In contrast to the decomposition in argon, three well-defined decomposition phases followed. At the first (T = 133 °C) the mass decreased by 8.6 %, then secondly by 25.7 %, with a maximum at T = 250 °C. The decomposition was clearly finished at T = 420 °C with a total mass loss of 44 %. This value fits quite well to the expected mass decrease from $[CH_3ZnOCH(CH_3)_2]_4$ to ZnO which is 41.63 %, and takes into account the previous sublimation of the heterocubane at low temperatures. The presence of oxygen has a profound impact on the solid-state synthesis. Instead of simultaneous sublimation and decomposition, sublimation was effectively suppressed, and three clear stages were identified. According to PXRD analysis, phase-pure ZnO was obtained (Figure 1d) and no substantial carbon contamination (below 1 %) was found in elemental analysis. It should be mentioned that in a separate experiment, the heterocubane was heated to four different temperatures (T_D = 150, 250, 350, and 450 °C) to investigate the particle formation process in SSS. Figure 1d shows the PXRD patterns for these four decomposition temperatures. In all cases ZnO was obtained, but the sample treated at only

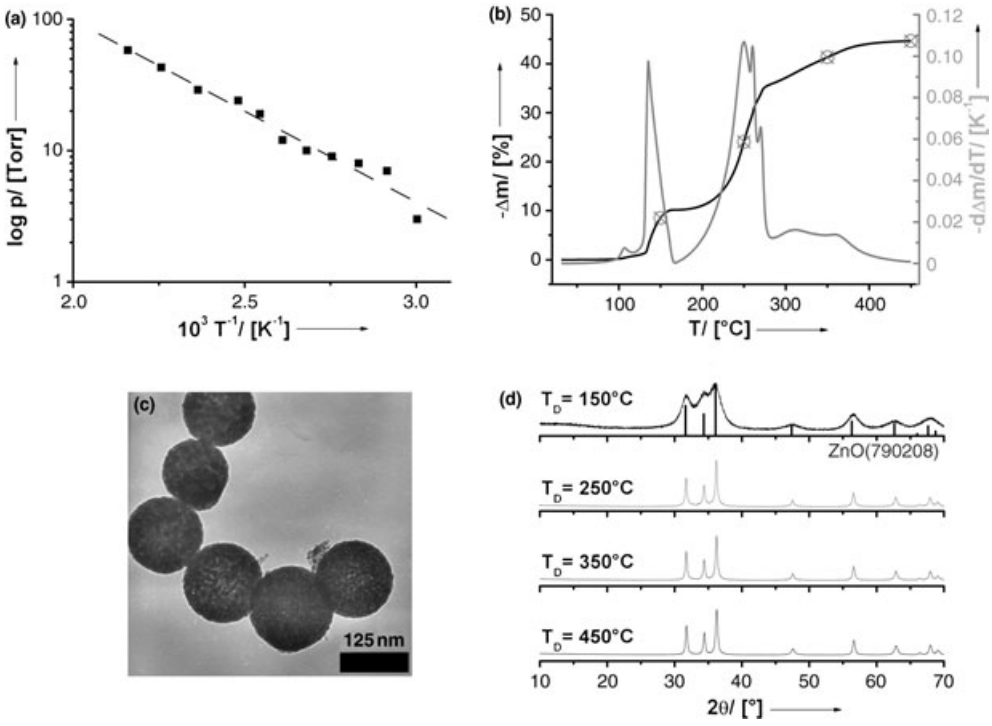

Figure 1. a) Results obtained from the determination of the vapor pressure of $[CH_3ZnOCH(CH_3)_2]_4$. b) TGA of the solid-state decomposition of $[CH_3ZnOCH(CH_3)_2]_4$ in an atmosphere containing 20 % oxygen. For better visibility of the different decomposition stages, the second axis shows the DTA results. The four crosshairs indicate the points where, in a separate experiment, ZnO samples were prepared which were then investigated with PXRD. c) TEM images of one of these materials (T = 350 °C) indicate unusual morphologies of ZnO nanoparticles aggregated to larger spheres. d) PXRD patterns of ZnO samples obtained at four different temperatures.

NANO MICRO small

150 °C is characterized by much broader diffraction patterns, which indicates the formation of nanoscale ZnO particles of average crystallite size (3.0 nm), as determined by the Scherrer equation (calculated from the full width at half maximum (FWHM)).[36] If the heterocubane is decomposed at 250 °C, particle growth to ≈25 nm occurs, and significant narrowing of the PXRD patterns can be observed. The size of the ZnO particles obtained from PXRD correlates well with TEM (Figure 1c). Interestingly, the single ≈25-nm ZnO nanoparticles are assembled into larger spherical aggregates of around 100-nm diameter. These results indicate that it is very difficult to obtain isolated, size-selected ZnO particles. Nevertheless, it can be concluded that to obtain pure ZnO, the heterocubane should react in an oxygen-containing atmosphere. Therefore, the solid-state decomposition is useful to define the conditions that should be applied in CVS.

Table 1. Experimental conditions, average crystallite size (D_c in nm) from PXRD, and mean particle diameter ($\bar{d}_p$ in nm) for ZnO particles (from TEM) obtained under different CVS conditions.

Sample code	Precursor temperature [°C]	Decomposition conditions (aerosol in 100 % N_2/20 % O_2 + 80 % N_2)		Average crystallite size (D_c) from PXRD [nm]	Mean particle diameter ($\bar{d}_p$) from TEM [nm]
		T [°C]	Residence time [s]		
NZ300	40–100	300 (100 % N_2)	23	≈6	≈6
OZ300	40–100	300	23	≈8	≈8
OZ500	40–140	500	17	≈10	≈9
OZ750	40–140	750	13	≈24	≈24
OZ900	40–100	900	11	≈30	≈29

To test the latter, in CVS the heterocubane was evaporated in flowing N_2 in a tube furnace, and oxygen was added to the aerosol directly in front of the decomposition furnace in which the heterocubane was finally decomposed at elevated temperatures (Figure 2). The decomposition under

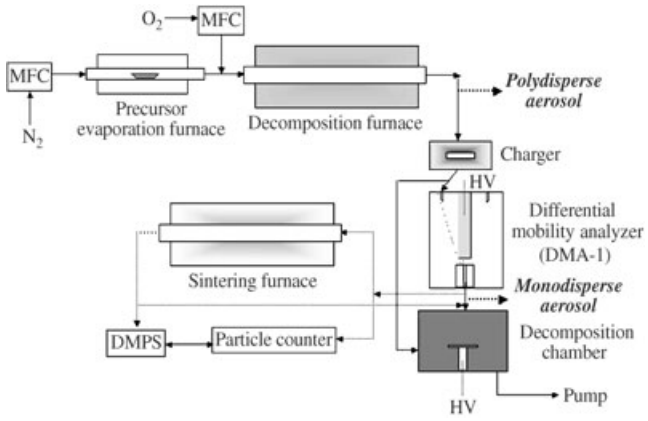

Figure 2. Schematic representation of the CVS setup.

CVS conditions is rather different from the solid-state decomposition, due to the fact that the precursor concentration is only at the parts per million (ppm) level; in the present study, the maximum precursor concentration was ≈12 ppm. A pronounced difference in particle-growth behavior can thus be expected.

Similar to the SSS experiments, the heterocubane was first treated in an inert atmosphere (N_2) to study the inherent ability of this particular precursor system, then the investigation of the effect of oxygen followed. The details of the CVS conditions are given in Table 1.

The PXRD pattern of the aerosol product obtained by decomposing the precursor at 300 °C under an inert atmosphere (NZ300; see Table 1) is shown in Figure 3a. The diffractogram clearly indicates the formation of nanocrystalline ZnO. The average crystallite size obtained for NZ300 is ≈6 nm. Figure 3c shows the TEM image of the polydisperse aerosol formed at 300 °C (NZ300) in nitrogen. The micrograph indicates the formation of aggregates containing several tens of primary particles with diameters in the range of 5–10 nm and a mean primary-particle diameter of ≈6 nm. Energy-dispersive X-ray (EDX) elemental analysis was performed on 20 different aggregates, which confirmed the presence of equal amounts of Zn:O (within the error limit of ±5 %). The PXRD and TEM results confirm the formation of nanocrystalline ZnO from the precursor under an inert atmosphere, which is different to the SSS route where carbon-rich materials were obtained. However, this only accounts for the material that was retrieved from the deposition chamber (Figure 2). Interestingly, during the inert gas decomposition experiment at 300 °C, a gray deposit was found on the wall of the decomposition tube, where the aerosol leaves the decomposition zone and the temperature decreases to about 150 °C. The PXRD pattern of this gray product can be identified as representing a mixture of elemental Zn and ZnO (Figure 3b). The TEM image of the powder (Figure 3d) shows rod- and beltlike morphologies having diameters within 30–100 nm and typical lengths of a few hundred nanometers to micrometers. The EDX measurements on these "whiskers" confirm the presence of Zn only, and the electron diffraction patterns (not shown) prove their crystallinity. To the best of our knowledge there is as yet no report on the formation of "Zn whiskers" at such a low temperature.[37] It can be suggested that the Zn whiskers grow by a vapor–solid (VS) mechanism caused by the high volatility of elemental zinc. This hypothesis is supported by findings recently published for Zn nanofibers prepared by evaporation of Zn powder.[37] The TEM image (Figure 3d) also shows the presence of agglomerated particles with lower contrast. EDX measurements on these agglomerated particles indicate a 1:1 atomic ratio of zinc and oxygen. These smaller particles can be attributed to ZnO, which was also found by PXRD. Therefore, ZnO and Zn did not form a nanocomposite but segregated on a macroscopic scale. The difference in distribution of Zn and ZnO can easily be explained by the different vapor pressures. Zinc remains in the gas phase inside the furnace because of its high vapor pressure and condenses at the coolest zone, the walls of the reactor, while exiting the decomposition furnace. Similar observations have been reported for metal

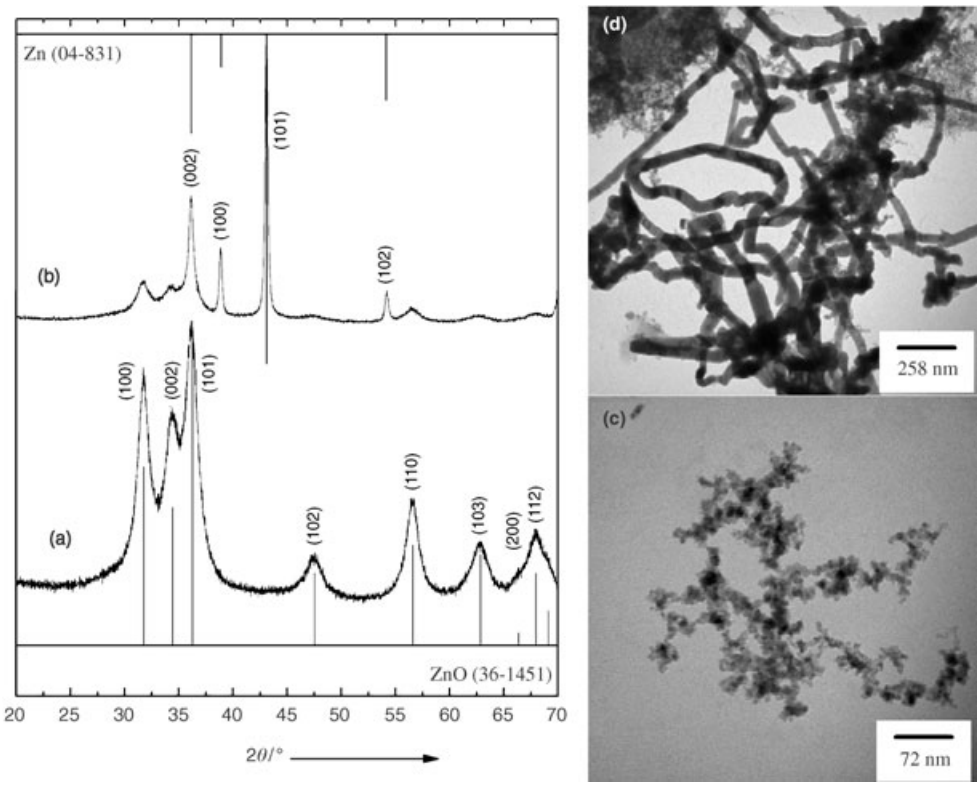

Figure 3. PXRD patterns and corresponding TEM images of CVS samples obtained in nitrogen (NZ300), collected in the deposition chamber (a, c) and at the cold end of the reactor (b, d). The reference diffraction patterns of ZnO and Zn are also given.

oxides with higher vapor pressures.[38,39] While the above results provide a reasonable explanation for the distribution of the two materials Zn and ZnO, the formation of Zn deserves particular attention as it is known that ZnO evaporates without homolytic cleavage, and, secondly, no formation of elemental zinc was found in the SSS. The results obtained from the SSS route are also in good agreement with MOCVD and solvothermal experiments using this precursor, in which the exclusive formation of ZnO was also found.[40]

Apparently, the precursor enables a second, yet not recognized, decomposition mechanism that results in the formation of elemental zinc. To address such a scenario in more detail, mass spectrometric studies were performed on the heterocubane. To this end, the heterocubane was ionized by electron ionization (70 eV), and the cations formed were accelerated to 8 keV kinetic energy and mass-selected by magnetic and electric sectors. Subsequently, the unimolecular and collision-induced fragmentations of the mass-selected cations were investigated. It was possible to derive the following fragmentation mechanism (Scheme 1): upon electron ionization of the neutral heterocubane, no molecular ion $[CH_3ZnOCH(CH_3)_2]_4^{+\cdot}$ can be observed. Instead, the heaviest fragment of dissociative ionization is $[(CH_3)_3Zn_4(OCH(CH_3)_2)_4]^+$, which corresponds to the loss of one methyl group. Unimolecular dissociation of mass-selected $[(CH_3)_3Zn_4(OCH(CH_3)_2)_4]^+$ leads to cluster cleavage and the elimination of a neutral monomer unit $[(CH_3)Zn(OCH(CH_3)_2)]$ concomitant with the Zn_3 cluster $[(CH_3)_2Zn_3(OCH(CH_3)_2)_3]^+$. Fragmentation of the latter occurs in two different ways: it either loses acetone, $(CH_3)_2CO$, or eliminates neutral MeZnH. Both products can be accounted for by involving an initial β-hydrogen transfer from the zinc-bound isopropoxy unit to the zinc atom, a process for which previous evidence exists in the gas-phase chemistry of transition-metal alkoxides.[41–45] Apparently, it is possible to a certain extent that the CH carbon atom attached to the oxygen atom can be oxidized from the formal oxidation state +0 (in the isopropoxide) to +2 (in acetone), accompanied by a hydride transfer to the Zn atom. Likewise, the fragment ion $[Me_2Zn_3(OCH(CH_3)_2)_2(H)]^+$ undergoes loss of neutral $[HZn(OCH(CH_3)_2)]$ concomitant with $[Me_2Zn_2(OCH(CH_3)_2)]^+$, which then shows loss of MeZnH as the major fragmentation pathway to afford the mononuclear

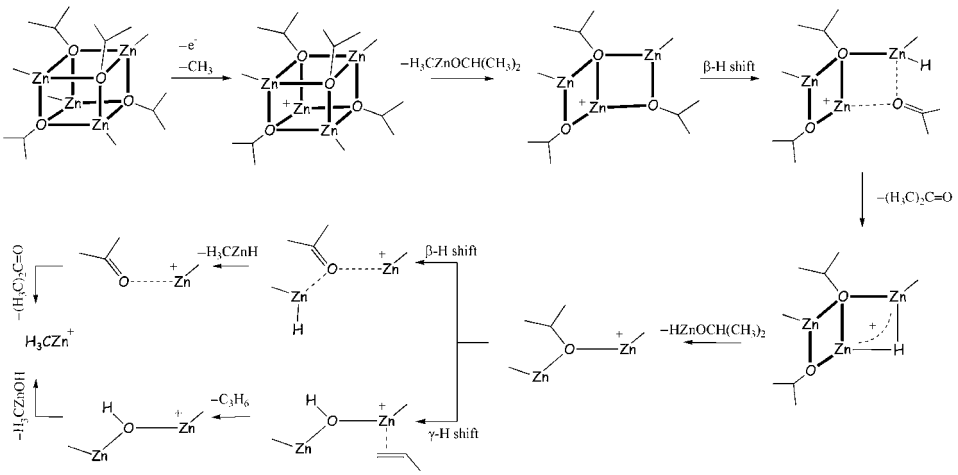

Scheme 1. Mechanistic investigation of the gas-phase decomposition of $[CH_3ZnOCH(CH_3)_2]_4$.

NANO MICRO small

cation $[MeZn(OC(CH_3)_2)]^+$. The latter finally eliminates acetone and furnishes CH_3ZnH. The generation of CH_3ZnH is remarkable because it can explain the formation of elemental Zn in the gas-phase decomposition of the heterocubane via the final decomposition step $CH_3ZnH \rightarrow Zn + CH_4$.

It may be questionable whether the proposed mechanism for the formation of Zn is valid for CVS, since the reaction cascades in the mass spectrometer are initiated by ionization. Therefore, (TGA-)MS measurements were performed in combination with the thermogravimetric decomposition of the heterocubane in an inert atmosphere discussed above. In fact, besides the expected volatile products propene and methane, which imply the formation of ZnO, a significant amount of acetone could also be detected. Hence, it seems very likely that the proposed mechanism is indeed responsible for the formation of elemental zinc under CVS conditions.

2.2 Particle Growth Investigation

The SSS gave phase-pure ZnO materials if prepared under an oxygen-containing atmosphere, therefore the CVS was conducted under analogous conditions (20% O_2). The PXRD patterns of the aerosol product obtained by decomposition of the precursor at different temperatures are shown in Figure 4a–d. The diffractograms clearly indicate the formation of hexagonal ZnO and the absence of any crystalline impurities in the samples. At relatively low decomposition temperatures ($T = 300\,°C$), the PXRD peaks are quite broad. With increasing decomposition temperatures, the widths of the peaks decrease in conjunction with a strong increase of their intensities. This observation indicates that the crystallite size of the product increases with higher decomposition temperatures (Table 1). Figure 4e–h shows the TEM images of the polydisperse aerosol formed at different temperatures under oxidizing conditions. The micrographs show the formation of aggregates containing several dozen primary particles in the OZ300 and OZ500 samples (Figure 4e and f).

Most of the primary particles obtained at these temperatures are in the range of 5–14 nm. Both the XRD and TEM results indicate that crystallite sizes do not change much with an increase in temperature from 300 to 500 °C, whereas a further increase of temperature from 500 to 750 °C leads to a large change in crystallite sizes. This is probably a result of sintering of the particles formed at high temperatures. Increasing the decomposition temperature further to 750 °C leads to the collapse of the aggregates and, due to sintering processes, formation of larger, compact particles (Figure 4g). Similar results were obtained at 900 °C (Figure 4h). The evolution of particles is apparently very different in SSS and CVS. While in SSS it seemed very difficult to control particle size and purity because of the low temperatures required for small particles, in CVS it appears that control over particle size can be obtained even at relatively high temperatures. This conclusion leads to the question whether or not the current system is suitable for an investigation of particle generation and growth processes in aerosols of metal oxides. We believe that this question is rather important because many approaches for preparing metal oxides involve aerosol methods. The PXRD and TEM results shown in Figure 4 demonstrate how ZnO particles evolve from small primary particles (≈8 nm in OZ300) to large aggregates, and then from aggregates to larger particles (≈29 nm in OZ900) due to thermal effects. To understand the nucleation, growth, aggregation, and sintering mechanism of the particles inside the decomposition furnace, more thorough investigations were performed and the details are give in this section.

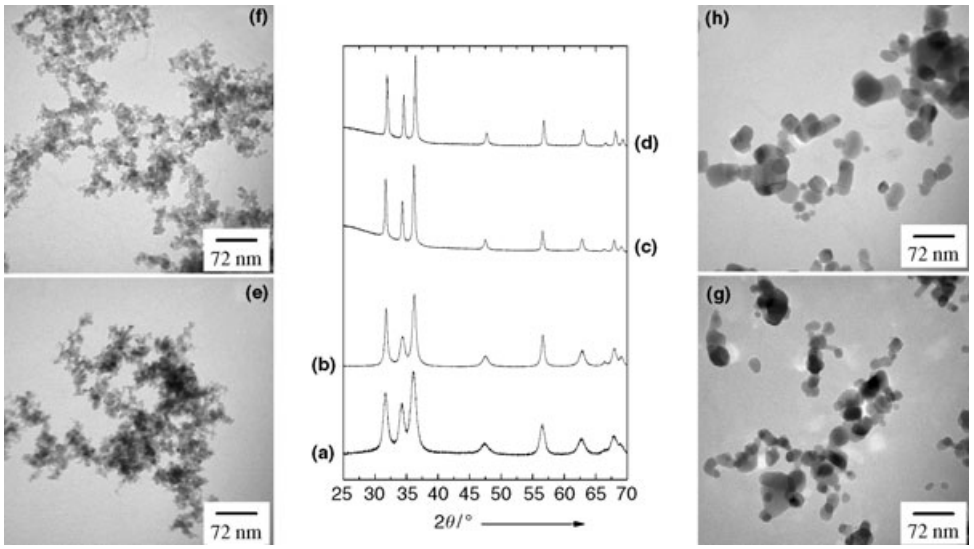

Figure 4. TEM images and PXRD patterns for CVS samples obtained at different temperatures in oxygen-containing atmospheres (20%). a), e) Samples at $T = 300\,°C$, b), f) at $T = 500\,°C$, c), g) at $T = 750\,°C$, and d), h) at $T = 900\,°C$.

Generally, the transformation of the organometallic precursor vapor to the final particles is a complex chemical and physical process. It involves vapor-phase chemical reaction, nucleation of the supersaturated vapor to form primary particles, primary-particle growth by vapor condensation and/or heterogeneous chemical reactions, coagulation by particle–particle collisions induced by their Brownian motion, and coalescence or sintering between particles.[46,47] For many metal oxides produced by oxidation of organometallic precursors using aerosol reactors or in flames, it has been

found that nucleation of the oxide species is virtually instantaneous due to the very rapid oxidation and high concentration of the precursor vapor, and only the physical coagulation and coalescence process determine the final particle morphology.[47,48] In the present study this was verified by increasing the precursor vapor pressure through increasing the evaporation temperature and keeping the decomposition furnace temperature constant at 300 °C to minimize any postsintering effect. A differential mobility analyzer (DMA) and condensation nucleus counter (CNC) were used to perform in situ measurements of the agglomerate mobility distribution with different precursor concentrations. When performing electrical mobility measurements, the classified mobility (mobility equivalent diameter, D_m) of the fractal-like aggregate is proportional to its projected area.[46,49] The results obtained from the mobility scan using the DMA and CNC showed that the geometric mean D_m values of the aggregates increase with an increase in precursor evaporation temperatures. The change in precursor vapor pressure (Figure 1a) does not result in any substantial change in the primary-particle diameters as proven by TEM. The results obtained from the change in D_m together with the unchanged primary size diameters indicate that only the number of primary particles in an individual aggregate increases. Thus, heterogeneous reactions do not play any role in the primary-particle growth and coagulation and/or coalescence determine the morphology of the final product.

The initial oxidation of the precursor vapor leads to the formation of highly reactive ZnO species, and collisions between them will take place due to Brownian motion. When the particle size is very small it is generally assumed that whenever two spherical particles collide they form a larger, spherical particle, that is, coalescence is instantaneous.[47] This is possible due to an enhanced surface diffusion coefficient, which results in a significant decrease in sintering time for clusters only few nanometers in size.[47,50] However, as the particles grow larger, this assumption fails, since the particle coalescence rate is no longer "instantaneous". Thus, beyond a critical size the particles stop growing by instantaneous coagulation–coalescence and fractal-like aggregates begin to form. This can be seen for samples OZ300 and OZ500 (Figure 5). The sintering of these agglomerated particles can also take place simultaneously in the decomposition furnace, although the extent of sintering is quite low up to 500 °C as discussed below. Upon increasing the temperature of the decomposition furnace, further sintering of the agglomerated particles takes place. This scenario accounts for the fully sintered particles observed at 750 and 900 °C (Figure 4g–h). Sintering of a material depends on many parameters, such as the temperature of the reactor, residence time inside the reactor, particle diameter, and fundamental physical properties of the particles. Thus, knowledge of the details of the time–temperature history in a reactor is very important. Although decomposition of the precursor at 750 or 900 °C gives sintered ZnO particles, it is still very difficult to separate out the sintering process from other processes such as chemical reactions, nucleation, or coagulation–coalescence. To obtain a more quantitative picture about the growth of aerosol particles of ZnO (and metal oxides in general), it is at least necessary to separate the chemical processes from the pure sintering processes in space and/or time. To this end, particles were generated at low temperature (at 300 °C), classified, and sintered in an-

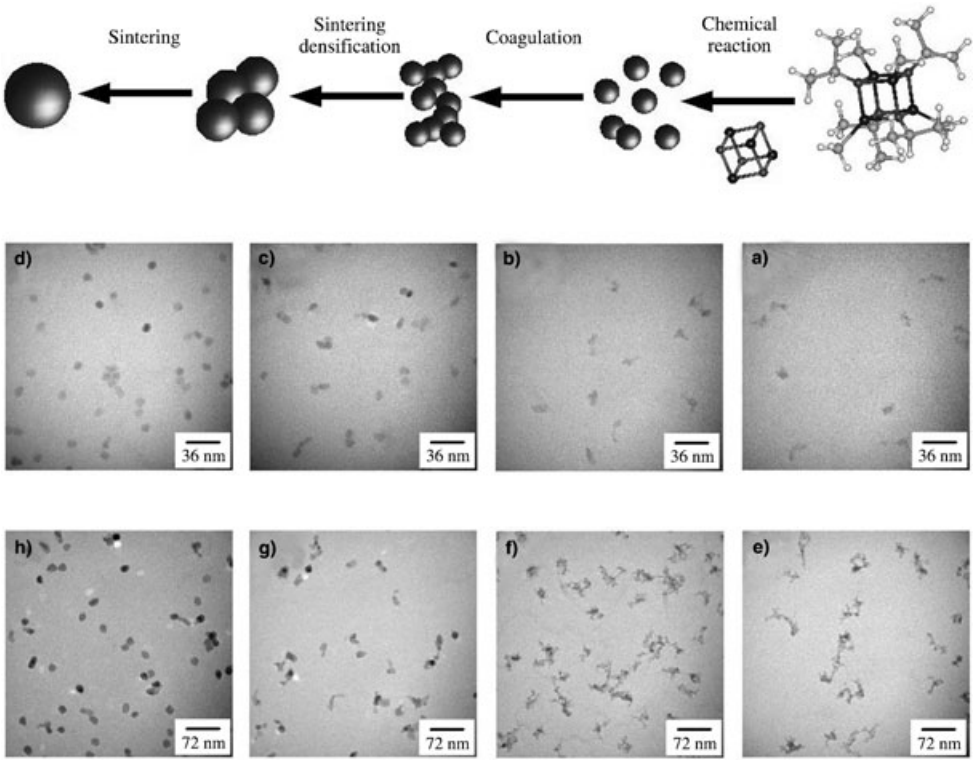

Figure 5. Left: a schematic representation of the morphological genesis of the CVS ZnO particles. The chemical "strip" of the heterocubane leads to highly reactive "Zn_4O_4" clusters (leaving organic groups are not shown). These species can be regarded as highly reactive ZnO monomers which, due to collisions between clusters, lead to the formation of primary particles of ZnO. These primary particles still have a very high interface energy, and undergo facile aggregation to larger particles. The primary particles fuse together at higher temperatures to form secondary particles via sintering densification. Finally, the secondary particles also sinter together to give the final single particle. a–d) TEM images for such a series of particle evolution steps for initial agglomerates with a D_m of 15 nm, and e–h) for initial agglomerates with a D_m of 30 nm.

other furnace at different temperatures (see Figure 2). Interaction among agglomerates in the sintering furnace, such as coagulation, can be neglected because of the sufficiently low concentration ($\approx 5\times10^4$ particles/cc) of the agglomerates in the gas phase. As the purity of the particles is very high as proven later, impurity effects in the sintering process can be neglected. Thus, the reduction of surface area (or D_m) and diameter of the particles can be measured (by DMA-CNC and TEM) without concern for other phenomena that would influence the sintering rate. Figure 5a–d show the changes of morphology of size-classified agglomerates of 15-nm mobility equivalent diameter (D_m), obtained by the first DMA, at different temperatures (300, 500, 750, and 900 °C). Figure 5e–h show a second example of sintering of agglomerates starting with a D_m of 30 nm. These images indicate that the agglomerates consist of primary particles which do not show any noticeable change in morphology till 500 °C. On increasing the sintering temperature to 750 °C, the agglomerates start to fuse into single spherical particles, and at 900 °C the particles are fully compact, that is, sintering is complete. The change of D_m of ZnO agglomerates with different sintering temperatures for four different initial sizes is shown in Figure 6. Below 500 °C, there is only a slight decrease in D_m. From 500 to 800 °C, there is a rapid decrease in D_m which is due to densification of the agglomerates. A further increase of the sintering temperature to 1000 °C leads to only a small change in D_m. In comparison, the TEM results show a very good correlation with D_m scan results. To understand the influence of temperature, residence time, and particle sizes on the sintering of the ZnO particles, it is important to identify the mechanism(s) contributing to the particle growth and compaction. Various stages and

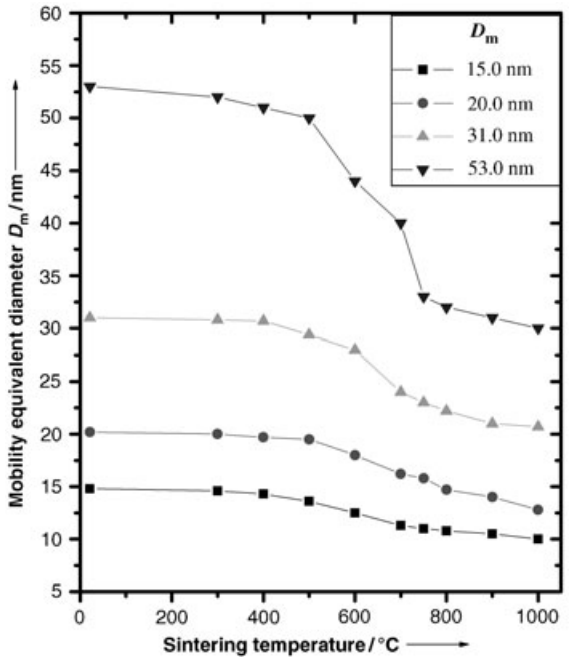

Figure 6. Change of mobility equivalent diameter (D_m) of ZnO agglomerates as a function of the sintering temperature for four different initial sizes.

mass transport mechanisms have been proposed to contribute to sintering.[51] The main mass-transport processes that determine solid-state sintering are surface diffusion, volume diffusion, grain-boundary diffusion, viscous flow, and evaporation–condensation.[51,52] The most accepted expression to calculate the characteristic sintering time, τ, is derived for the initial stage of sintering from the two-sphere model with the assumption that it holds true for all stages of sintering.[46–48,51–53] To calculate τ, it is important to determine the rate-controlling transport mechanism(s) for sintering. ZnO has a melting point of 1975 °C, and it is therefore rather unlikely that viscous flow plays any significant role in the sintering mechanism for $T \leq 900$ °C as in our experiments. The evaporation–condensation mechanism can also be neglected due to the very low vapor pressure of ZnO in this temperature range.[54] Surface diffusion plays an important role only in the initial stage of neck formation, but it does not contribute to the densification and, thus, its contribution to sintering was neglected, in agreement with the literature.[53,54] Therefore, in all subsequent calculations only grain-boundary and volume diffusions were further considered as the sintering mechanism. To determine the time needed for two ZnO particles to sinter by grain-boundary diffusion (τ_{GB}), the relation given by Kobata et al. was used,[55] which was successfully applied previously for various other systems:[46,48,56,57]

$$\tau_{GB} = \frac{(0.013 k_B T r_i^4)}{b D_{GB} \gamma v} \quad (1)$$

where k_B is the Boltzmann constant, T is the sintering furnace temperature, r_i is the radius of the primary particles, b is the grain-boundary width, D_{GB} is the grain-boundary diffusion coefficient, γ is the surface tension, and v is the atomic volume. The above relation has been derived for $(2l/D_{pi}) = 0.83$, where l is the neck radius and D_{pi} the initial primary-particle diameter, and assumes that the grain-boundary width remains constant during the coalescence process. The literature values of bD_{GB},[58] γ,[59,60] and v are listed in Table 2. To the best of our knowledge, there is only one report on the grain-boundary diffusion coefficients for ZnO.[58] Based on that report, it was possible to calculate τ_{GB} values after extrapolating the grain-boundary diffusion coefficient in the studied temperature range. The grain-boundary diffusion coefficient of zinc was used for calculation because of the much higher diffusivity value of zinc

Table 2. Physical properties of ZnO used in the present calculations.

Properties	Values	References
Melting point (T_m, bulk)	1975 °C	[56]
Molecular weight (M)	81.37	[56]
Density (ρ)	5.6 g cm^{-3}	[56]
Atomic volume (v)	2.4×10^{-29} m^3	
Surface tension (γ)	0.735 J m^{-2}	[60,61]
bD_{GB} (see text)	1.59×10^{-12} exp [−(235.14 KJ)/RT] m^3 s	[59]
D_{VD} (see text)	1.7×10^{-7} exp [−(256.34 kJ)/RT] m^2 s	[59]

compared to that of oxygen.[58,61] Figure 7a shows the dependence of the primary-particle diameter ($D_{pi}=2r_i$) on τ_{GB} as a function of temperature. The experimental residence times in the sintering furnace at 25 °C (4.6 s) and 1000 °C (1.1 s) are also shown in Figure 7a and it should be noted that the residence time decreases with an increase in sintering temperature. τ_{GB} values increase with an increase in primary-particle diameter (Figure 7a) and decrease with increase in sintering temperature. Figure 7a reveals that, with the present experimental residence time, sintering due to grain-boundary diffusion cannot be observed below 500 °C for particles >6 nm in diameter. Since the mean primary-particle diameter of ZnO agglomerates obtained at 300 °C is ≈8 nm (see Table 1), and according to Figure 7a, these can be sintered at 750 °C, which is consistent with the experimental findings (see Figures 5 and 6). Accordingly, grain-boundary diffusion can be identified as a reasonable mechanism responsible for sintering of ZnO primary particles. The characteristic sintering time of coalescence by volume diffusion, τ_{VD}, was calculated using the relation given by Friedlander et al.:[62]

$$\tau_{VD} = \frac{(k_B T r_i^3)}{(16 D_{VD} \gamma v)} \quad (2)$$

where D_{VD} is the volume diffusion coefficient of the diffusing species. Values of the different physical parameters are given in Table 2. Several groups have reported the diffusivity of zinc in ZnO;[63] for the present work we used the Arrhenius equation recently reported by Nogueira at al., which is in good agreement with results from other groups.[58] Figure 7b shows the primary-particle diameter (D_{pi}) dependency of τ_{VD} as a function of temperature. The experimental residence times in the sintering furnace at 25 °C and 1000 °C are also shown for comparison. Figure 7b shows that primary particles with a diameter of 8 nm cannot be sintered by diffusional sintering at 750 °C or even at 900 °C within the present experimental residence times. Comparison of Figure 7a and b implies that, for a certain primary-particle diameter and at a certain temperature, τ_{VD} exceeds τ_{GB} by a factor of 10^5. These results suggest that the grain-boundary diffusion of zinc controlled the rate of diffusional sintering in the present study. Recently, Hynes et al.[54] reported that 95–98 % theoretical density was achieved on isothermal sintering of nanophase undoped ZnO at 650–700 °C for 40 min. This result is in good agreement with the proposed model in the present study. In conclusion, the results concerning the sintering of the ZnO aerosol presented above demonstrate that it is possible not only to nicely control the size of the semiconductor nanoparticles, but also to understand their formation on a much more fundamental basis.

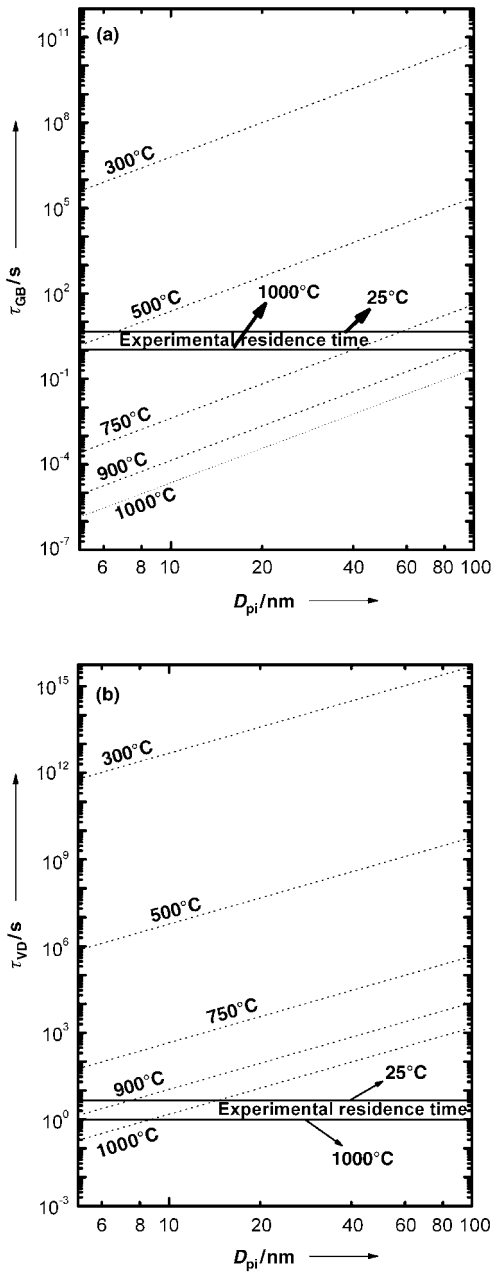

Figure 7. Change of the characteristic sintering time as a function of temperature and initial primary-particle diameter (D_{pi}), a) for grain-boundary diffusion τ_{GB} and b) for volume diffusion τ_{VD}.

2.3 Investigation of Sample Purity

It has already been mentioned that an additional advantage of the gas-phase synthesis in comparison to the solid-state synthesis could be that products of higher purity can be obtained. It is clear that not only the morphology (size and shape) of semiconductors will influence their properties, but also the compositional and microstructural purity is of extraordinary importance. Therefore, the purity of the materials obtained from CVS was studied and compared to that of the SSS samples. However, it appears meaningless to compare samples according to the temperature of preparation because concentration, as well as mobility and residence time, is extremely different in the CVS and SSS routes. Therefore, samples of similar ZnO particle size were compared with each other. Figure 8a shows the ^{13}C magic-angle spinning (MAS) NMR spectrum of an SSS sample

NANO MICRO small

with average particle size of 25 nm. After 20000 scans, weak but nevertheless clear signals at 180.7, 169.0, and 20.0 ppm were observed. We assign the deep-field signals to the occurrence of surface-bound carboxylate species. Even upon treatment at higher temperature, it was difficult to remove these carboxylates, while the high-field signal disappeared. We therefore, attribute the signal at 20 ppm to C–H species. It has already been shown above that in CVS it is possible to go to significantly higher temperatures than for SSS while particle growth is restricted. Accordingly, sample OZ750 (Table 1) also possesses an average particle size of ≈25 nm, and can be compared best to the SSS sample. Comparing Figure 8a and b demonstrates that there is no detectable signal for ^{13}C in the CVS sample. This finding indicates that the CVS sample is free of organic impurities.

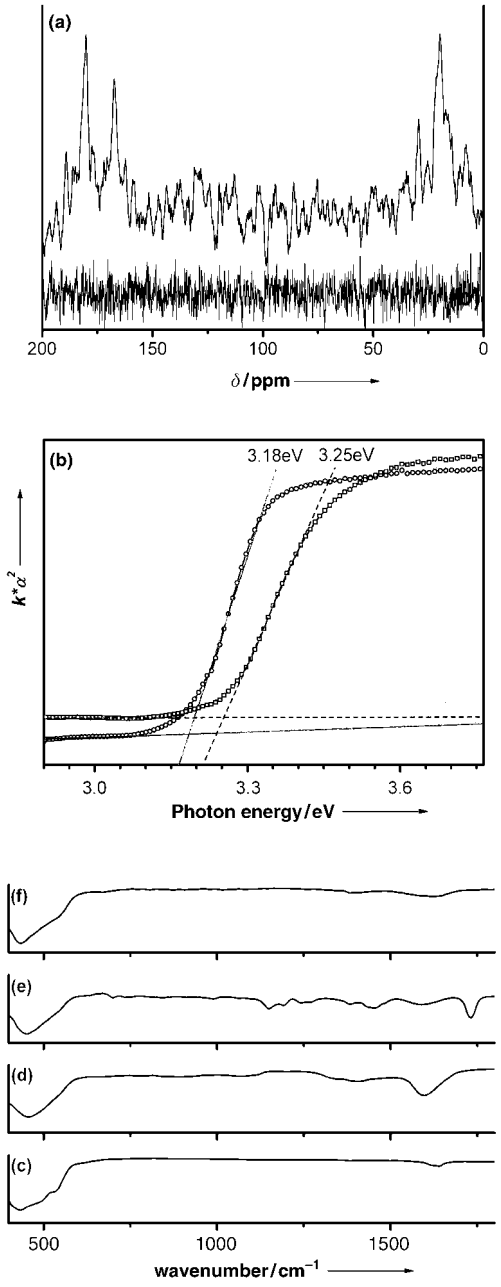

Figure 8. a) ^{13}C MAS NMR spectra of ZnO samples of comparable particle size (≈25 nm) via SSS (upper curve) in comparison to CVS (OZ750; lower curve). b) UV/Vis spectra of two samples obtained by CVS. c–f) FTIR spectra: c) commercial ZnO as reference; d) SSS sample; e) CVS sample (OZ300); f) CVS sample (OZ750). g) UV/Vis spectra of CVS samples with two different particle sizes (5 and 12 nm).

To support this conclusion, FTIR spectra of different samples were recorded and referenced to the spectrum of commercial ZnO (Figure 8c) with the most intense band at $\tilde{\nu}=440\ cm^{-1}$. The IR spectra of the SSS sample (Figure 8d) confirm the presence of carboxylate species by the strong band at $1600\ cm^{-1}$, in good agreement with the ^{13}C MAS NMR studies. Two CVS samples were measured for comparison. One sample (Figure 8e) was prepared at a temperature (OZ300) comparable to that of the SSS sample. Various bands at $\tilde{\nu}=1730$, 1588, 1452, 1387, 1245, 1192, 1149, 698, and $445\ cm^{-1}$ are present. Hence, a temperature of 300 °C is insufficient for removal of all remaining organic impurities from the ZnO sample. A key advantage of the CVS procedure is therefore that it enables higher process temperatures. In fact, the CVS sample prepared at 750 °C was free of organic impurities (Figure 8f).

Finally, two samples of different particle size (5 and 12 nm) obtained by CVS were investigated by UV/Vis spectroscopy in reflection mode (see Figure 8g). The determination of the bandgap revealed 3.18 eV for the 5-nm sample and 3.25 eV for the 12-nm sample. The red-shift of the absorption edge in comparison to the literature value of ZnO (3.30 eV) cannot be explained by quantum size effects,[64] but is reasonably explained by the occurrence of shallow donor levels introduced by impurity atoms such as carbon.

Room-temperature photoluminescence (PL) spectra were recorded to investigate the presence of oxygen defects. Depending on the preparation technique, ZnO is known to show two main emission bands under photoexcitation. The first band in the ultraviolet range (around 3.25 eV) is generally attributed to recombination of free or bound excitons close to the bandgap.[65] The second and much broader emission band mainly covers the green part of the visible spectrum (2.3–2.6 eV) and is therefore usually called "green band emission". The origin of this visible PL signal has been related to various types of defects, such as singly ionized oxygen vacancies,[66] antisite oxygen,[67] or donor–acceptor recombination.[68,69]

In this context it is an interesting question whether the relative and the absolute intensities of both near-bandgap and defect luminescence can be controlled by the external parameters of the synthesis. Therefore, we measured the PL spectra of four different samples (OZ300, OZ500, OZ750, and OZ900) which are shown in Figure 9. It can be seen that the total PL intensity of the near-bandgap transition I_B strongly increases (by more than a factor of 25) with increasing sintering temperature T. At the same time the total amount of defect luminescence I_D decreases. As a result of both, the ratio of defects to near-bandgap luminescence I_D/I_B decreases strongly with T (inset of Figure 9). We believe that the observed behavior of the PL properties is directly related to the sintering process of the nanoparti-

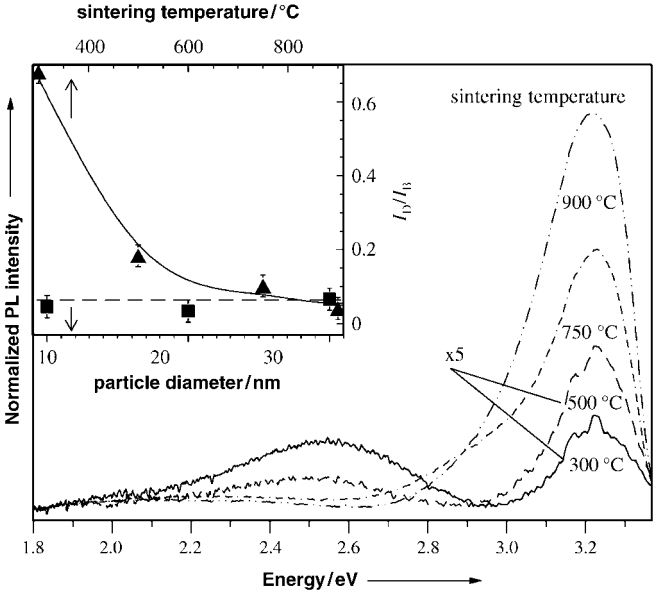

Figure 9. Photoluminescence spectra of polydisperse ZnO nanoparticles synthesized by CVS at varying sintering temperatures. Inset: ratio of defect to band-to-band intensities over sintering temperature and particle size for monodisperse particles sintered at 900 °C.

cles and can be controlled thereby. At a temperature of 900 °C highly crystalline ZnO nanoparticles were obtained (see Figure 5). The PL spectra show virtually no defect luminescence and a strong transition close to the bandgap. On the other hand, for temperatures below 500 °C the sintering process is strongly inhibited and no annealing of defects can occur. Thus, agglomerates of particles with a high defect density are being probed instead of single nanocrystals. These defects can cause both green luminescence and nonradiative recombination that reduces the overall PL intensity.

It is important to mention that the particle diameter varied with sintering temperature T. As can be seen in Table 1, the average diameter of the primary particles increases from 8 nm for $T = 300$ °C to 29 nm for $T = 900$ °C. An increase of the particle diameter leads to a lower surface-to-volume ratio and might therefore contribute to the observed changes in the PL signal with T. To ensure that this is not the dominant effect in our samples, we measured size-classified nanoparticles synthesized at $T = 900$ °C with diameters of 10, 20, and 30 nm. As can be seen in the inset of Figure 9, no significant variation of I_D/I_B with particle size was found, which clearly demonstrates that the sintering temperature rather than the particle size is mainly responsible for the present observations.

3. Conclusions

The goal of the current work was to develop a method of preparing isolated ZnO nanoparticles with adjustable size and high purity. It was shown that the heterocubane cluster $[CH_3ZnOCH(CH_3)_2]_4$ is a suitable precursor to obtain high-purity ZnO under oxidizing conditions. However, we learned that it was very difficult to control the size of the nanoparticles by solid-state synthesis, and that instead of isolated particles, agglomerates were always obtained. We therefore concentrated on the gas-phase synthesis (CVS) of ZnO. The gas-phase mechanism of decomposition of the heterocubane precursor was investigated in detail, and it was shown that in the absence of O_2 elemental zinc is produced due to the elimination of acetone and other organic groups from the cluster framework. This scenario was further supported by MS/MS experiments, which clearly showed that the heterocubane tends to eliminate acetone. In addition to the morphological control over ZnO, it was possible to obtain ZnO particles free of any impurities. The samples obtained from the solid-state decomposition were applied as a reference system, in which it was not possible to obtain pure and defect-free materials.

However, it was seen that structural defects can also influence the physical properties of ZnO. As the main factor we identified the presence of oxygen defects in the ZnO lattice. In combination with photoluminescence spectra the factors influencing such oxygen defects could be analyzed. It was shown that it is also possible to obtain defect-free ZnO materials by CVS.

4. Experimental Section

The volatile single-source precursor used in this method was synthesized by performing all reactions under inert conditions with the Schlenck technique. A Schlenck flask containing toluene (50 mL) and a 2 M $Zn(CH_3)_2$ solution in toluene (10 mL) was cooled to −78 °C. Dry isopropanol (1.2 g) was slowly added and, after warming to room temperature, a clear solution was obtained. The solvent was removed in vacuo to give pure $[CH_3ZnOCH(CH_3)_2]_4$ (2.3 g; 90 %). ^{1}H NMR (250 MHz, $[D_6]$benzene, 25 °C, TMS): $\delta = 0$ (s, 3H, $ZnCH_3$), 1.45 (d, 6H, $C(CH_3)_2$), 4.21 ppm (sept, 1H, CH).

The gas-phase decomposition of the precursor was performed at normal pressure of pure nitrogen and 20 % (by volume) oxygen, respectively, at different temperatures. The experimental setup used for CVS is depicted in Figure 2. The precursor was evaporated in a tube furnace at 40–100 °C and then carried to another tube furnace by nitrogen at a flow rate of 1.5 L min^{-1}. For oxidative conditions, N_2 (1.2 L min^{-1}) was passed over the precursor and O_2 (0.3 L min^{-1}) was applied. Decomposition of the precursor, particle formation and subsequent growth, and sintering of the formed particles took place in a second furnace at elevated temperatures. Details of the CVS conditions are given in Table 1. The particles formed after decomposition remained as an aerosol in the gas phase, and were then passed through an α-source (^{241}Am) to charge the particles. The polydisperse charged particles were then either deposited directly or passed through a differential mobility analyzer (NANO-DMA, TSI, Minneapolis, USA) for size classification and then deposited with ≈100 % efficiency on a suitable substrate (TEM grid or Si

NANO MICRO small

wafer) using an electrostatic precipitator.[70] A condensation nucleus counter (CNC, TSI, Model 3022, Minneapolis, USA) was used to monitor the aerosol number concentration. The polydisperse aerosol produced was also examined with the differential-mobility particle sizing technique (DMPS, TSI, Model 3081) for particle size distribution with respect to time, precursor evaporation temperature, and precursor decomposition temperature.

PXRD analyses of all powder samples and deposited particles were performed on a Bruker AXS D8 Advance instrument using $Cu_{K\alpha}$ radiation ($\lambda = 1.5418$ Å) and a position-sensitive detector (PSD). Thermogravimetric analyses (differential thermal analysis (DTA)–TGA) of the precursor were carried out with a thermogravimetric setup from Rubotherm in the range 25 to 900 °C in argon and oxygen. A linear rate of heating of 5 K min^{-1} was maintained during all the measurements. Conventional transmission electron microscopy (TEM) was performed on a Philips CM12 microscope (LaB_6 filament, 120 kV, twin lens) equipped with an energy-dispersive X-ray spectrometer (EDX, type Oxford Link). The powder samples obtained by solid-state decomposition were suspended in cyclohexane using an ultrasonic bath for 5 min and then left to dry on a carbon-coated TEM grid. FTIR spectra were recorded with a Bruker Vector 22 spectrometer (KBr pellets). UV/Vis spectra were recorded using a Perkin–Elmer Lambda 20 spectrometer equipped with a reflecting sphere, Labsphere RSA-PE-20. Solid-state NMR spectra were recorded using a Bruker DRX 400 spectrometer.

The optical properties of ZnO nanoparticles synthesized by CVS were studied by room-temperature photoluminescence spectroscopy. The samples were excited with the 351-nm UV line of an argon ion laser. The emission was dispersed by a 300-mm monochromator and recorded by a thermoelectrically cooled charge-coupled device (CCD) camera. To avoid saturation of possible defect luminescence, low excitation densities were used ($P_{Laser} = 2.8$ W cm^{-2}).

The gas-phase experiments were performed with a modified VG ZAB/HF/AMD 604 four-sector mass spectrometer of BEBE configuration (B stands for magnetic and E for electric sector), which has been described elsewhere.[71] In brief, cations were generated by electron ionization (EI) of $[CH_3ZnOCH(CH_3)_2]_4$ introduced via a solid probe. After acceleration to a kinetic energy of 8 keV, the ions of interest were mass-selected and subjected to metastable ion (MI) and collisional activation (CA) studies. MI spectra of B(1)/E(1) mass-selected ions were recorded by detection of the charged fragments formed unimolecularly in the field-free region between E(1) and B(2) by scanning the latter sector. CA spectra were recorded in the same manner using helium (80 % transmission) as a stationary collision gas. All spectra reported refer to mass selection of the pure ^{64}Zn isotopes; losses of neutral zinc compounds were confirmed by the spectra of the ions containing one ^{66}Zn atom. The vapor pressure of the heterocubane was measured by Dr. P. Schmidt (TU Dresden, Germany) using a membrane-zero manometer as described elsewhere.[34,35]

Acknowledgment

We thank Dr. P. Schmidt (TU Dresden, Germany) for the determination of the vapor pressure of the heterocubane. Dr. W. Schmidt (Max-Planck Institute for Coal Research, Germany) is gratefully acknowledged for the TGA–MS measurements. We thank Deutsche Forschungsgemeinschaft (SPP 1119, CVS of nanocrystalline metal oxide and silicate films by pyrolysis of molecular metal alkoxides and metal siloxides) for financial support. We also thank H. Zähres (University Duisburg-Essen, Germany) for the TEM measurements.

[1] *Acc. Chem. Res.* **1999**, *32*, Special Issue on Nanoscale Materials.
[2] *Chem. Mater.* **1996**, *8*, Special Issue on Nanostructured Materials.
[3] Y. N. Xia, P. D. Yang, Y. G. Sun, Y. Y. Wu, B. Mayers, B. Gates, Y. D. Yin, F. Kim, Y. Q. Yan, *Adv. Mater.* **2003**, *15*, 353.
[4] L. M. Liz-Marzán, D. J. Norris, *MRS Bull.* **2001**, *26*, 981.
[5] P. Moriarty, *Rep. Prog. Phys.* **2001**, *64*, 297.
[6] H. Gleiter, *Acta Mater.* **2000**, *48*, 1.
[7] D. C. Look, B. Claftin, *Phys. Status Solidi B* **2004**, *241*, 624.
[8] B. K. Meyer, H. Alves, D. M. Hofmann, W. Kriegseis, D. Forster, F. Bertram, J. Christen, A. Hoffmann, M. Strassburg, M. Dworzak, U. Haboeck, A. V. Rodina, *Phys. Status Solidi B* **2004**, *241*, 231.
[9] D. C. Look, D. C. Reynolds, C. W. Litton, R. L. Jones, D. B. Eason, G. Cantwell, *Appl. Phys. Lett.* **2002**, *81*, 1830.
[10] M. A. Martinez, J. Herrero, M. T. Gutierrez, *Sol. Energy Mater. Sol. Cells* **1997**, *45*, 75.
[11] N. A. Anderson, X. Ai, T. Q. Lian, *J. Phys. Chem. B* **2003**, *107*, 14414.
[12] K. Keis, J. Lindgren, S. E. Lindquist, A. Hagfeldt, *Langmuir* **2000**, *16*, 4688.
[13] Y. Darici, P. H. Holloway, J. Sebastian, T. Trottier, S. Jones, J. Rodriquez, *J. Vac. Sci. Technol. A* **1999**, *17*, 692.
[14] E. Monroy, F. Omnes, F. Calle, *Semicond. Sci. Technol.* **2003**, *18*, R33.
[15] H. M. Lin, S. J. Tzeng, P. J. Hsiau, W. L. Tsai, *Nanostruct. Mater.* **1998**, *10*, 465.
[16] D. R. Clarke, *J. Am. Ceram. Soc.* **1999**, *82*, 485.
[17] H. Wilmer, M. Kurtz, K. V. Klementiev, O. P. Tkachenko, W. Grünert, O. Hinrichsen, A. Birkner, S. Rabe, K. Merz, M. Driess, C. Wöll, M. Muhler, *Phys. Chem. Chem. Phys.* **2003**, *5*, 4736.
[18] S. J. Pearton, D. P. Norton, K. Ip, Y. W. Heo, T. Steiner, *J. Vac. Sci. Technol.* **2004**, *22*, 932.
[19] Z. L. Wang, *J. Phys. Condens. Matter* **2004**, *16*, R829.
[20] R. Viswanatha, S. Sapra, B. Satpati, P. V. Satyam, B. N. Dev, D. D. Sarma, *J. Mater. Chem.* **2004**, *14*, 661.
[21] G. Rodriguez-Gattorno, P. Santiago-Jacinto, L. Rendon-Vazquez, J. Nemeth, I. Dekany, D. Diaz, *J. Phys. Chem. B* **2003**, *107*, 12597.
[22] Z. S. Hu, G. Oskam, P. C. Searson, *J. Colloid Interface Sci.* **2003**, *263*, 454.
[23] M. Shim, P. Guyot-Sionnest, *J. Am. Chem. Soc.* **2001**, *123*, 11651.
[24] E. A. Meulenkamp, *J. Phys. Chem. B* **1998**, *102*, 5566.
[25] V. Noack, A. Eychmuller, *Chem. Mater.* **2002**, *14*, 1411.
[26] F. E. Kruis, H. Fissan, A. Peled, *J. Aerosol Sci.* **1998**, *29*, 511.
[27] T. Tani, L. Madler, S. E. Pratsinis, *J. Nanopart. Res.* **2002**, *4*, 337.
[28] R. Wu, C. S. Xie, H. Xia, J. H. Hu, A. H. Wang, *J. Cryst. Growth* **2000**, *217*, 274.
[29] A. Roy, S. Polarz, S. Rabe, B. Rellinghaus, H. Zahres, F. E. Kruis, M. Driess, *Chem. Eur. J.* **2004**, *10*, 1565.

[30] S. Seifried, M. Winterer, H. Hahn, *Chem. Vap. Deposition* **2000**, *6*, 239.
[31] M. Driess, K. Merz, R. Schoenen, S. Rabe, F. E. Kruis, A. Roy, A. Birkner, *CR Chim.* **2003**, *6*, 273.
[32] H. Kleinwechter, C. Janzen, J. Knipping, H. Wiggers, P. Roth, *J. Mater. Sci.* **2002**, *37*, 4349.
[33] C. G. Kim, K. W. Sung, T. M. Chung, D. Y. Jung, Y. Kim, *Chem. Commun.* **2003**, 2068.
[34] P. Schmidt, H. Oppermann, *Z. Naturforsch. B* **2000**, *55*, 603.
[35] P. Schmidt, H. Oppermann, N. Soger, M. Binnewies, A. N. Rykov, K. O. Znamenkov, A. N. Kuznetsov, B. A. Popovkin, *Z. Anorg. Allg. Chem.* **2000**, *626*, 2515.
[36] E. Lifshin, *Characterization of Materials*, Wiley-VCH, Weinheim, **1999**.
[37] X. S. Peng, L. D. Zhang, G. W. Meng, X. Y. Yuan, Y. Lin, Y. T. Tian, *J. Phys. D* **2003**, *36*, L35.
[38] Y. Xiong, S. W. Lyons, T. T. Kodas, S. E. Pratsinis, *J. Am. Ceram. Soc.* **1995**, *78*, 2490.
[39] S. W. Lyons, Y. Xiong, T. T. Ward, T. T. Kodas, S. E. Pratsinis, *J. Mater. Res.* **1992**, *7*, 3333.
[40] J. Auld, D. J. Houlton, A. C. Jones, S. A. Rushworth, M. A. Malik, P. Obrien, G. W. Critchlow, *J. Mater. Chem.* **1994**, *4*, 1249.
[41] C. J. Cassady, B. S. Freiser, *J. Am. Chem. Soc.* **1985**, *107*, 1566.
[42] C. J. Cassady, B. S. Freiser, *J. Am. Chem. Soc.* **1985**, *107*, 1573.
[43] C. J. Cassady, B. S. Freiser, S. W. McElvany, J. Allison, *J. Am. Chem. Soc.* **1984**, *106*, 6125.
[44] D. Schröder, H. Schwarz, *Angew. Chem.* **1990**, *102*, 925; *Angew. Chem. Int. Ed. Engl.* **1990**, *29*, 910.
[45] A. Fiedler, D. Schroder, H. Schwarz, B. L. Tjelta, P. B. Armentrout, *J. Am. Chem. Soc.* **1996**, *118*, 5047.
[46] T. Seto, M. Shimada, K. Okuyama, *Aerosol Sci. Technol.* **1995**, *23*, 183.
[47] Y. Xing, D. E. Rosner, *J. Nanopart. Res.* **1999**, *1*, 277.
[48] Y. Xing, U. O. Koylu, D. E. Rosner, *Combust. Flame* **1996**, *107*, 85.
[49] K. Nakaso, T. Fujimoto, T. Seto, M. Shimada, K. Okuyama, M. M. Lunden, *Aerosol Sci. Technol.* **2001**, *35*, 929.
[50] S. Tsantilis, H. Briesen, S. E. Pratsinis, *Aerosol Sci. Technol.* **2001**, *34*, 237.
[51] R. M. German, *Sintering Theory and Practice*, Wiley, New York, **1996**.
[52] W. S. Coblenz, J. M. Dynys, R. M. Cannon, R. L. Coble, *Mater. Sci. Res.* **1980**, *13*, 141.
[53] F. E. Kruis, K. A. Kusters, S. E. Pratsinis, B. Scarlett, *Aerosol Sci. Technol.* **1993**, *19*, 514.
[54] A. P. Hynes, R. H. Doremus, R. W. Siegel, *J. Am. Ceram. Soc.* **2002**, *85*, 1979.
[55] A. Kobata, K. Kausakabe, S. Morooka, *AIChE J.* **1991**, *37*, 347.
[56] M. Shimada, T. Seto, K. Okuyama, *J. Chem. Eng. Jpn.* **1994**, *27*, 795.
[57] K. Nakaso, M. Shimada, K. Okuyama, K. Deppert, *J. Aerosol Sci.* **2002**, *33*, 1061.
[58] M. A. S. N. Nogueira, W. B. Ferraz, A. C. S. Sabioni, *Mater. Res.* **2003**, *6*, 167.
[59] J.-G. Li, *J. Mater. Sci. Lett.* **1994**, *13*, 400.
[60] J. Z. Jiang, J. S. Olsen, L. Gerward, D. Frost, D. Rubie, J. Peyronneau, *Europhys. Lett.* **2000**, *50*, 48.
[61] A. C. S. Sabioni, M. J. F. Ramosm, W. B. Ferraz, *Mater. Res.* **2003**, *6*, 173.
[62] S. K. Friedlander, M. K. Wu, *Phys. Rev. B* **1994**, *49*, 3622.
[63] G. W. Tomlins, J. L. Routbort, T. O. Mason, *J. Appl. Phys.* **2000**, *87*, 117.
[64] A. Wood, M. Giersig, M. Hilgendorff, A. Vilas-Campos, L. M. Liz-Marzan, P. Mulvaney, *Aust. J. Chem.* **2003**, *56*, 1051.
[65] D. M. Bagnall, Y. F. Chen, Z. Zhu, T. Yao, M. Y. Shen, T. Goto, *Appl. Phys. Lett.* **1998**, *73*, 1038.
[66] K. Vanheusden, W. L. Warren, C. H. Seager, D. R. Tallant, J. A. Voigt, B. E. Gnade, *J. Appl. Phys.* **1996**, *79*, 7983.
[67] B. X. Lin, Z. X. Fu, Y. B. Jia, *Appl. Phys. Lett.* **2001**, *79*, 943.
[68] D. C. Reynolds, D. C. Look, B. Jogai, *J. Appl. Phys.* **2001**, *89*, 6189.
[69] S. A. Studenikin, M. Cocivera, *J. Appl. Phys.* **2002**, *91*, 5060.
[70] F. E. Kruis, K. Nielsch, H. Fissan, B. Rellinghaus, E. F. Wassermann, *Appl. Phys. Lett.* **1998**, *73*, 547.
[71] C. A. Schalley, M. Dieterle, D. Schroder, H. Schwarz, E. Uggerud, *Int. J. Mass Spectrom. Ion Processes* **1997**, *163*, 101.

Received: September 28, 2004
Revised: January 26, 2005

